Comparison of gating dynamics of different IP_3R channels with immune algorithm searching for channel parameter distributions

2016 Phys. Biol. 13 056005

(http://iopscience.iop.org/1478-3975/13/5/056005)

Physical Biology

PAPER

Comparison of gating dynamics of different IP_3R channels with immune algorithm searching for channel parameter distributions

Xiuhong Cai[1], **Xiang Li**[1], **Hong Qi**[2], **Fang Wei**[1], **Jianyong Chen**[3] **and Jianwei Shuai**[1,4]

[1] Department of Physics, Xiamen University, Xiamen 361000, People's Republic of China
[2] Complex Systems Research Center, Shanxi University, Taiyuan 030006, People's Republic of China
[3] College of Computer Science & Software Engineering, Shenzhen University, Shenzhen 518000, People's Republic of China
[4] State Key Laboratory of Cellular Stress Biology, Innovation Center for Cell Signaling Network, Xiamen University, Xiamen, 361102, People's Republic of China

E-mail: jianweishuai@xmu.edu.cn

Keywords: channel, calcium signaling, immune algorithm

RECEIVED
3 June 2015

REVISED
16 August 2016

ACCEPTED FOR PUBLICATION
31 August 2016

PUBLISHED
17 October 2016

Abstract

The gating properties of the inositol 1, 4, 5-trisphosphate (IP_3) receptor (IP_3R) are determined by the binding and unbinding capability of Ca^{2+} ions and IP_3 messengers. With the patch clamp experiments, the stationary properties have been discussed for *Xenopus* oocyte type-1 IP_3R (Oo-IP_3R1), type-3 IP_3R (Oo-IP_3R3) and *Spodoptera frugiperda* IP_3R (Sf-IP_3R). In this paper, in order to provide insights about the relation between the observed gating characteristics and the gating parameters in different IP_3Rs, we apply the immune algorithm to fit the parameters of a modified DeYoung–Keizer model. By comparing the fitting parameter distributions of three IP_3Rs, we suggest that the three types of IP_3Rs have the similar open sensitivity in responding to IP_3. The Oo-IP_3R3 channel is easy to open in responding to low Ca^{2+} concentration, while Sf-IP_3R channel is easily inhibited in responding to high Ca^{2+} concentration. We also show that the IP_3 binding rate is not a sensitive parameter for stationary gating dynamics for three IP_3Rs, but the inhibitory Ca^{2+} binding/unbinding rates are sensitive parameters for gating dynamics for both Oo-IP_3R1 and Oo-IP_3R3 channels. Such differences may be important in generating the spatially and temporally complex Ca^{2+} oscillations in cells. Our study also demonstrates that the immune algorithm can be applied for model parameter searching in biological systems.

1. Introduction

Elevation of intracellular Ca^{2+} level represents a ubiquitous signaling pathway, controlling a variety of cellular functions including proliferation, learning memory, metabolism, gene transcription, and apoptosis [1, 2]. In almost all kinds of cells, Ca^{2+} ions are released from the endoplasmic reticulum (ER) into the cytosol through inositol 1, 4, 5-trisphosphate (IP_3) receptor (IP_3R) channels [3]. The IP_3R is a tetrameric Ca^{2+} selective channel [3, 4]. Three IP_3R subtypes (IP_3R1, IP_3R2, IP_3R3) have been identified in mammals [4]. The regulatory properties of IP_3R channels have been studied extensively with IP_3R1 in experiments [5]. The IP_3Rs are activated by IP_3 and also controlled by cytosolic Ca^{2+} concentration ($[Ca^{2+}]$) with both positive and negative feedbacks [6].

Experimentally, membrane patch clamp technique has been mainly applied to measure the current changes of IP_3R channels to investigate its open and closing activities [6–9]. These patch clamp recordings have been first performed in lipid bilayers [10, 11], which is not *in vivo* situation. Later, it has been shown that the IP_3R channel activity can be measured by using nuclear patch clamp in its native nuclear membrane. Different stationary properties, including the open probability, mean open time and mean closing time, under different concentrations of Ca^{2+} and IP_3 have been measured systematically with endogenous Xenopus oocyte type-1 IP_3R (Oo-IP_3R1) [6], recombinant rat type-3 IP_3R expressed in oocytes (Oo-IP_3R3) [7] and endogenous *Spodoptera frugiperda* IP_3R (Sf $-IP_3R$) [8]. With these experimental data an interesting question remains: what processes of Ca^{2+} and IP_3 binding to and unbinding from IP_3Rs can be revealed for these different IP_3R channels? Understanding the ligand binding and unbinding properties of IP_3Rs is important for studying cellular Ca^{2+} signal.

In order to discuss the channel gating properties, various models have been suggested to explain the patch clamp recordings of IP_3R channels and to investigate the oscillation kinetics of Ca^{2+} signal. Mak *et al* proposed an allosteric four-plus-two-conformation model, in which it was postulated that an IP_3R channel is composed of four IP_3R monomers and each IP_3R monomer has one IP_3 binding site and three different Ca^{2+} binding sites [7]. Specific kinetic model for the type-2 IP_3R has been considered by Sneyd and Dufour, assuming the whole channel as an entirety instead of the four-subunit construction [12]. Dupont and Combettes developed phenomenological model accounting for the distinct steady-state behaviors of IP_3Rs [13] to discuss their effects on Ca^{2+} signals, but this model is not based on the underlying molecular processes related to IP_3 and Ca^{2+} binding. DeYoung and Keizer assumed that an IP_3R channel is made up of three identical and independent subunits. For each subunit, there are an IP_3 binding site, an activating Ca^{2+} binding site and an inhibitory Ca^{2+} binding site [14]. Shuai *et al* built up a model based on the DeYoung–Keizer model (DYK model), taking four independent subunits into account and considering that IP_3R channel opens through configuration change [15]. Shuai *et al* [16] also compared different models and discussed their various fitting efforts with the Oo-IP_3R1 patch clamp experimental recordings. Ullah *et al* established a model consists of a Markov chain with nine close states and three open states, which accounts for experimentally observed gating behaviors of single native Sf-IP_3R channel [17]. Among these models, DYK model [14, 18] has been widely applied in Ca^{2+} signaling simulation.

In these modeling studies, the researchers typically considered an IP_3R channel with a set of fixed model parameters to discuss the patch clamp data of IP_3R channel or Ca^{2+} signaling experiments. Mathematically, various sets of model parameters can be chosen to fit to a group of experimental data within a certain matching error. As a result, one can obtain a probability distribution of fitting values for each model parameter. Such distributions actually reveal the robustness and reliability of the model parameters. However, there has been little discussion on the robustness and reliability of IP_3R model parameters.

In the present work, we fit the modified DYK IP_3R model parameters with experimental data of Oo-IP_3R1, Sf-IP_3R and Oo-IP_3R3, including open probability, mean open time and mean close time with the artificial immune algorithm. The artificial immune algorithm is an intelligent algorithm inspired by the principles and processes of biological immune system. For specific reactivity, an organism responds to an antigen invasion swiftly and creates specific antibody to eliminate the antigen. The immune algorithm is inspired by this specific reactivity. The objective functions correspond to the antigens. Once the objective functions (antigens) are given, the algorithm (organism) will generate the specific vector (antibody) by a series of cloning, recombination and mutation processes (see methods section for detail).

Artificial immune system has been applied to solve various application problems, including fault detection [19], pattern recognition [20], computer security [21], etc. Especially, it has been substantially studied for solving multi-objective optimization problems (MOPs). The first reported approach that directly uses artificial immune system to solve MOPs was presented by Yoo and Hajela [22]. The immune concept of antibody–antigen affinity is incorporated into a standard genetic algorithm to modify the fitness assignment. Afterward, many multi-objective immune algorithms (MOIAs) are presented to solve MOPs. Based on the special features provided by artificial immune system, they can be classified into three categories. The first kind of MOIAs is based on clonal selection approach, which uses the cloning principle to get the copies of superior antibodies that are chosen to have the better affinities [23–25]. In this category, a representative algorithm is the hybrid immune multi-objective optimization algorithm (HIMO) (see methods section for detail) [24]. In the second category, the immune network theory is applied to evolve the population and to maintain the population diversity [26–28]. The last category is proposed to combine an immune system and another heuristic algorithm in order to embed some advantageous operators of the heuristic algorithm into MOIAs [29–32].

In this work we apply the HIMO algorithm to fit the parameters of the modified DYK IP_3R model to nuclear membrane patch clamp experimental data to investigate the relation between the observed gating characteristics and the gating parameters of IP_3Rs. As a result, a number of optimal fitting parameters are found automatically for the IP_3R model by applying the immune algorithm. Based on the parameter distributions, the robustness of IP_3R model parameters is studied. Furthermore, by comparing the parameter distributions of Oo-IP_3R1, Oo-IP_3R3 and Sf-IP_3R, we reveal the different channel dynamics of these three IP_3Rs.

2. Method and model

2.1. Immune algorithm

First, we introduce the artificial immune algorithm applied in our study. The HIMO algorithm aims to obtain the approximate minima of multi-objective functions promptly [24, 32], which is described as below with the HIMO flowchart shown in figure 1.

First, we set the fitting parameters of $x_1, x_2, \ldots, x_k$ as the fitting vector $X = (x_1, x_2, \ldots, x_k)$, i.e., the antibody. For the case of multiple objective functions, the optimization goal is to find a set of fitting vectors X to satisfy the constraints, i.e. to make each objective function smaller than a desired critical number

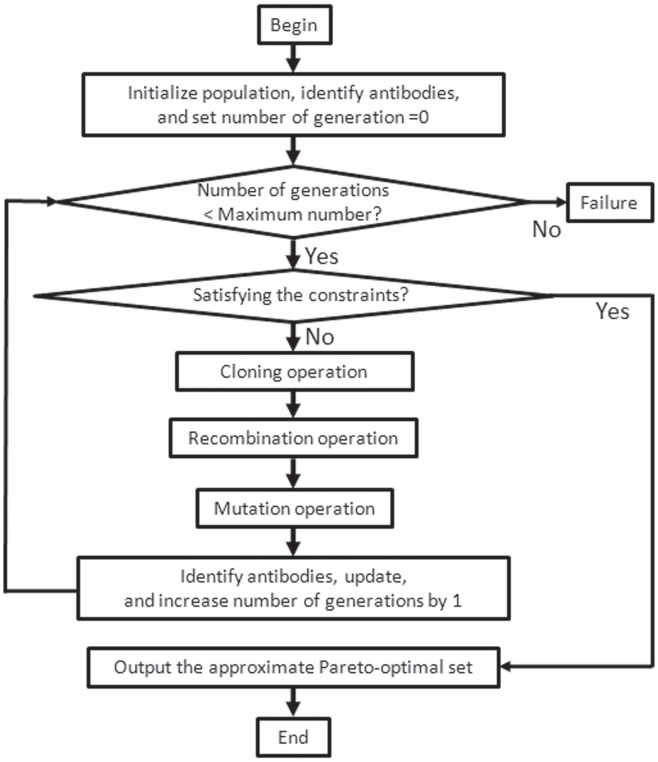

Figure 1. The flowchart of HIMO algorithm.

individually. The fitting vectors that satisfy the constraint conditions are termed the optimal vectors. Considering the vector of objective function $F(X)$:

$$F(X)_{X\in G} = (f_1(X), f_2(X), \cdots f_m(X)), \tag{1}$$

where $f_i(X)$ is the objective function ($i = 1, 2, \ldots, m$), m is the number of objective functions and the set G is the possible domain of vector X. In our example discussed below, the objective functions are the three relative mismatch functions between modeling and experimental results and the constraint condition is simply to consider that the sum of the three objective functions should be smaller than a critical number.

At the beginning of the algorithm, one needs to randomly initialize a set of antibodies, i.e., the population of fitting vectors. Then according to the objective function, one searches for the optimal antibodies that satisfy the constraints of objective function vector by clone, recombination and mutation operations at each generation [24, 32], which will be described in detail below. In our simulation, the maximal number of generations is 10^6, which is a large enough number reasonably determined with calculation time. We always obtain the optimal antibodies before reaching the maximal number of generations.

3. Clone operation

In HIMO algorithm, the clone operation of antibodies is considered first. The cloning number of an antibody is according to its affinity which is typically related to a set of small objective functions. The larger the affinity, the more clones are generated for that antibody.

We suppose a population set $A = (X^1, X^2, \ldots, X^n)$, where X^i is an antibody and n is the total number of antibodies. In our simulation, we consider 100 antibodies, i.e. 100 fitting vectors. The cloning number that we want to clone with the antibody X^i is defined as $q^i (i = 1, 2, \ldots, n)$:

$$q^i = n_* \frac{Q(X^i)}{\sum_{j=1}^{n} Q(X^j)}, \tag{2}$$

where $Q(X^i)$ is the affinity of antibody X^i, defined as:

$$Q(X^i) = \sum_{j=1}^{m} \frac{Q_j(X^i)}{f_j^{\max} - f_j^{\min}} \tag{3}$$

in which $f_j^{\max}$ and $f_j^{\min}$ are the maximum and minimum values of jth objective functions, respectively, and the function $Q_j(X^i)$ is given as

$$Q_j(X^i) = \begin{cases} \infty, & f_j(X^i) = f_j(X^k)_{\min} \text{ or} \\ & \times f_j(X^i) = f_j(X^k)_{\max}, \\ (f_j(X^k) - f_j(X^l))_{\min}, & \text{otherwise} \\ \text{Here, } k, l = 1, 2, \ldots, n, & \text{and } k \neq l \neq i. \end{cases} \tag{4}$$

Instead of applying $Q_j(X^i) = \infty$ in the simulation, we actually set $Q_j(X^i)$ as the twofold of maximal affinity.

4. Recombination operation

Next, we consider the recombination operation to generate new antibodies from the old antibodies in order to avoid getting into local optimal solutions for antibodies (i.e. the fitting vectors).

HIMO applies binary crossover operator [33] to generate two new fitting vectors (i.e. two new antibodies) from two old antibodies of $X^0 = (x_1^0, x_2^0, \ldots, x_n^0)$ and $X^1 = (x_1^1, x_2^1, \ldots, x_n^1)$:

$$\begin{aligned} y_i^0 &= 0.5*[(1+\beta)*x_i^0 + (1-\beta)*x_i^1], \\ y_i^1 &= 0.5*[(1-\beta)*x_i^0 + (1+\beta)*x_i^1], \end{aligned} \tag{5}$$

where y_i^0 and y_i^1 are the variables of new antibodies of Y^0 and Y^1, and β is the parameter defined by following random equations:

$$\beta = \begin{cases} [\text{ran}*\alpha]^{\frac{1}{\eta+1}}, & \text{ran} \leqslant \dfrac{1}{\alpha} \\ \left[\dfrac{1}{2-\text{ran}*\alpha}\right]^{\frac{1}{\eta+1}}, & \text{ran} > \dfrac{1}{\alpha} \end{cases} \tag{6}$$

in which η is a crossover-distribution factor which is set as 15 normally, ran is a random number, and α is given by

$$\alpha = 2 - \left(\frac{1}{1+2*\dfrac{(y_{iu} - (x_i^0, x_i^1)_{\max}, (x_i^0, x_i^1)_{\min} - y_{id})_{\min}}{(x_i^0, x_i^1)_{\max} - (x_i^0, x_i^1)_{\min}}}\right)^{\eta+1}, \tag{7}$$

where y_{iu} and y_{id} are the upper boundary and the lower boundary of the ith variable.

5. Mutation operation

Then, we introduce the mutation operation for each antibody at each generation in order for antibodies to jump out of local optimal solutions. For mutation, there are two kinds of mutation operators, i.e. the polynomial mutation and the Gaussian mutation. HIMO combines both mutations, which is called GP-HM operator [32].

HIMO uses dynamic mutation possibility p_m to decide the possibility of each antibody for mutation, which is defined by:

$$p_m = \begin{cases} (1+p)*p_m^{\min} - 2*p*p_m^{\min}*\left(\dfrac{g}{g_{\max}}\right), & g < \dfrac{g_{\max}}{2}, \\ p_m^{\min}, & g > \dfrac{g_{\max}}{2}, \end{cases} \tag{8}$$

where $p_m^{\min}$ is default minimum mutation possibility, p is a default parameter to control the number of antibodies to mutate, g is the current generation, and $g_{\max}$ is default maximum generation.

For antibody $X = (x_1, x_2, \ldots, x_n)$, the GP-HM mutation operator is defined by:

$$x_i' = x_i + \Delta*(y_{iu} - y_{id}),\ i = 1, 2, \ldots, n, \tag{9}$$

where x_i' is the new ith variable of antibody X after mutation.

For polynomial mutation, Δ is given by

$$\Delta = \begin{cases} \left[2r_i + (1+2r_i)*\left(\dfrac{(y_{iu} - x_i,\ x_i - y_{id})_{\max}}{y_{iu} - y_{id}}\right)^{\frac{1}{\mu+1}}\right] - 1, & r_i < 0.5, \\ 1 - \left[2(1-r_i) + 2(r_i - 0.5)*\left(\dfrac{(y_{iu} - x_i,\ x_i - y_{id})_{\max}}{y_{iu} - y_{id}}\right)^{\mu+1}\right]^{\frac{1}{\mu+1}} - 1, & r_i \geqslant 0.5, \end{cases} \tag{10}$$

where μ is the mutation-distribution factor which is set as 20 normally. For Gaussian mutation, Δ is defined as

$$\Delta = 0.1*N(0,1). \tag{11}$$

HIMO uses a self-adaption parameter s to control the transfer of these two mutations:

$$s = \left(x - y*\frac{g}{g_{\max}}\right)*\frac{Q(X^i) - Q_{\min}}{Q_{\max} - Q_{\min}}. \tag{12}$$

After the clone, recombination and mutation operations, HIMO identifies the fitting vectors, saves and updates them. The multi-objective function optimization aims to search the optimal vector set satisfying the constraints to make each objective function as small as required, i.e., the approximate Pareto-optimal set [24, 32].

5.1. IP_3R channel model

There are different IP_3R channel models suggested by now [12–18]. In the paper we adopt a modified version of the DYK model [14], a simple IP_3R model widely applied in numerical simulation of intracellular Ca^{2+} signals, in which each model parameter has a direct meaning related to ligand (Ca^{2+} or IP_3) binding to or

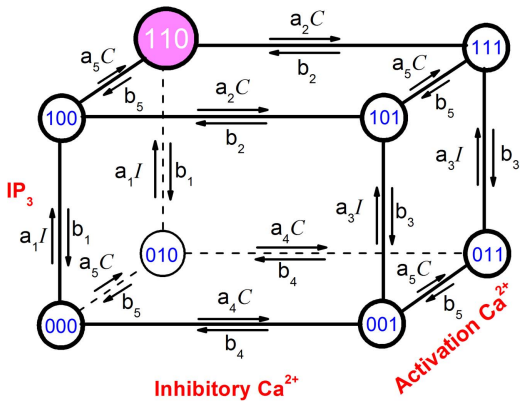

Figure 2. The schematic diagram of the state transitions for a DYK IP_3R subunit. In each subunit, there are one IP_3 binding site, one activating Ca^{2+} binding site and one inhibitory Ca^{2+} binding site.

unbinding from the channel. In our modified DYK model, an IP_3R channel is composed of four identical and independent subunits. In each subunit, there are one IP_3 binding site, one activating Ca^{2+} binding site and one inhibitory Ca^{2+} binding site, as shown in figure 2. We use *ijk* to denote the state of each subunit, where *i* represents the IP_3 binding site, *j* the activating Ca^{2+} binding site, and *k* the inhibitory Ca^{2+} binding site. The bound state of each binding site is represented by 1, whereas the empty state by 0. Thus each subunit has 8 possible states (figure 2). The subunit is active when it is occupied only by IP_3 and activating Ca^{2+}, i.e., state 110. In the model we suppose that once three out of the four subunits are in activated state, the channel will become open [34, 35].

There are ten parameters in the IP_3R model, in which a_i represents the binding rate constant, b_i the unbinding rate constant, so the dissociation constant is given by $K_i = b_i/a_i$. According to the thermodynamic constraint of detailed balance, we have $K_1K_2 = K_3K_4$. In this paper, C and I represent the concentrations of Ca^{2+} and IP_3, respectively.

With the deterministic matrix transition method [16], the stationary properties, i.e., open probability P_o, mean open time τ_o and mean close time τ_c, of IP_3R channel can be expressed as a function of the binding/unbinding parameters of the model. Supposing that the probability of an IP_3R subunit in state 000 is $q_{000} = 1$, the probability of a subunit in state *ijk*, i.e. q_{ijk}, is then given by the ratio between the product of forward rates and the product of backward rates along the shortest binding or unbinding path relative to the state 000. For example, the probability q_{110} of the open state (110) is given as

$$q_{110} = \frac{IC}{K_1K_5}. \tag{13}$$

Then we normalize the equilibrium probability for state *ijk* and obtain

$$w_{ijk} = \frac{q_{ijk}}{Z}, \tag{14}$$

where $Z = \sum q_{ijk}$, i.e.

$$Z = 1 + \frac{C}{K_4} + \frac{C}{K_5} + \frac{C}{K_4}\frac{C}{K_5} + \frac{I}{K_1} + \frac{I}{K_1}\frac{C}{K_2} + \frac{I}{K_1}\frac{C}{K_5} + \frac{I}{K_1}\frac{C}{K_2}\frac{C}{K_5}. \tag{15}$$

Therefore, the normalized equilibrium probability for state (110) is

$$w_{110} = \frac{I}{K_1}\frac{C}{K_5}\frac{1}{Z}. \tag{16}$$

Because the channel opens when three or four subunits are in activated state (110), the channel open probability is then given by

$$P_O = P_{4O} + P_{3O} = w_{110}^4 + 4w_{110}^3(1 - w_{110}), \tag{17}$$

where $P_{4O} = w_{110}^4$ and $P_{3O} = 4w_{110}^3(1 - w_{110})$ represent the probabilities when four and three subunits are in active state, respectively.

The equilibrium probability flux is written as follow:

$$J = 3P_{3O}(b_1 + b_5 + a_2C). \tag{18}$$

Thus the mean open time and mean close time are given by

$$\tau_O = \frac{P_O}{J}, \tag{19}$$

and

$$\tau_C = \frac{1 - P_O}{J}. \tag{20}$$

According to above formulas, we can calculate P_o, τ_o and τ_c at different I and C.

5.2. Multi-objective functions

Because the objective of the HIMO algorithm is to find out the approximate minima of multi-objective functions, we set the relative mismatch between modeling and experimental values as our objective functions. The experimental results are P_O, τ_o and τ_c of Oo-IP_3R1 [6], Oo-IP_3R3 [7] and Sf-IP_3R [8] obtained by nuclear patch clamp technique. The three relative mismatch functions between modeling and experimental results are defined as:

$$W_{P_o} = \frac{\sum_{I,C}|P_O^{expt}(I, C) - P_O^{mod}(I, C)|}{\sum_{I,C}P_O^{expt}(I, C)}, \tag{21}$$

$$W_{\tau_o} = \frac{\sum_{I,C}|\log(\tau_O^{expt}(I, C)) - \log(\tau_O^{mod}(I, C))|}{\sum_{I,C}\log(\tau_O^{expt}(I, C))}, \tag{22}$$

and

$$W_{\tau_c} = \frac{\sum_{I,C}|\log(\tau_C^{expt}(I, C)) - \log(\tau_C^{mod}(I, C))|}{\sum_{I,C}\log(\tau_C^{expt}(I, C))}. \tag{23}$$

Applying these equations to HIMO algorithm, we set above three mismatch functions as the objective

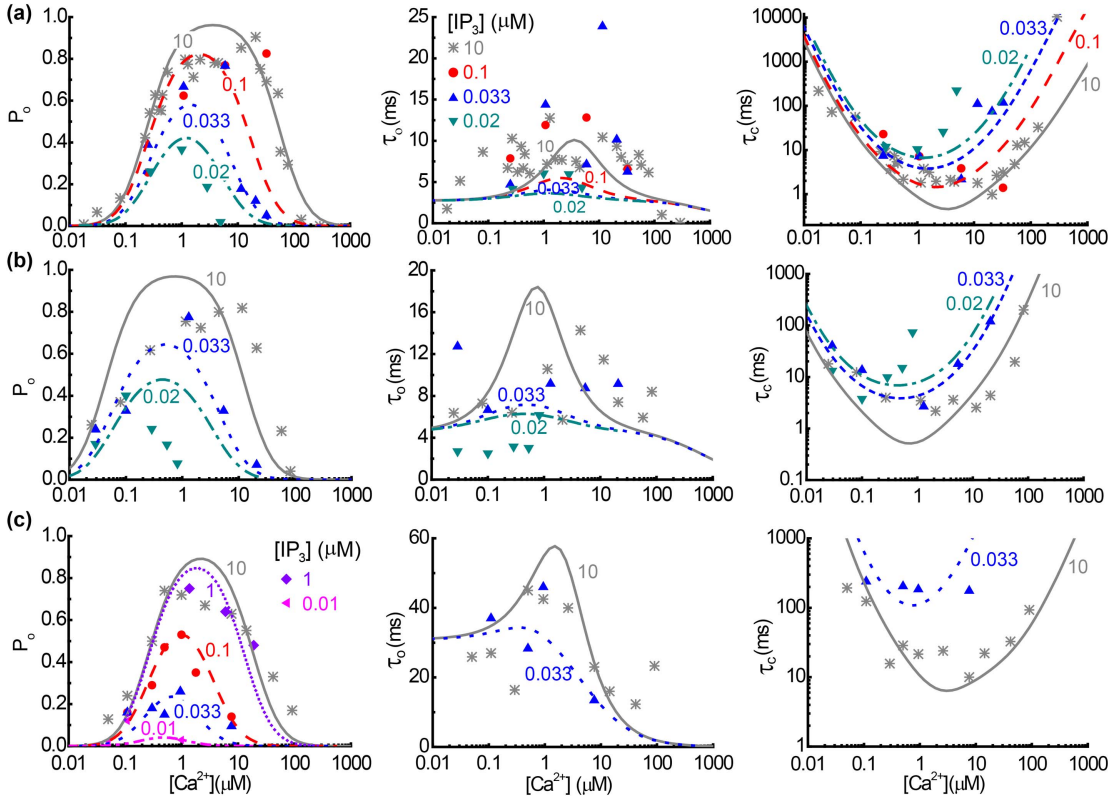

Figure 3. The modeling fittings to experimental data of the open probability P_o (left column), the mean open time τ_o and (middle column) and the mean closing time τ_c (right column) as a function of $[Ca^{2+}]$ for different $[IP_3]$ for (a) Oo-IP$_3$R1, (b) Oo-IP$_3$R3, and (c) Sf-IP$_3$R, respectively. The fitting parameters (a) for Oo-IP$_3$R1 are $K_1 = 0.0074, K_2 = 82.5, K_3 = 0.23, K_5 = 0.16, a_1 = 1 \times 10^{-4}$, $a_2 = 1.0 \times 10^{-4}, a_5 = 0.76$; (b) for Oo-IP$_3$R3 are $K_1 = 0.0093, K_2 = 18.65, K_3 = 0.06, K_5 = 0.029, a_1 = 0.0021, a_2 = 1.0 \times 10^{-4}$, $a_5 = 2.48$; and (c) for Sf-IP$_3$R are $K_1 = 0.013, K_2 = 27.6, K_3 = 0.49, K_5 = 0.18, a_1 = 0.61, a_2 = 0.0018, a_5 = 0.017$. Units of parameter are μM for K_i and $\mu M^{-1}ms^{-1}$ for a_i (same in all the following figures).

functions $f_1(X), f_2(X)$ and $f_3(X)$ with X the fitting vector of the objective functions. Thus we have $F(X) = (W_{P_O}(X), W_{\tau_O}(X), W_{\tau_C}(X))$ for equation (1).

For IP$_3$R model, there are 10 parameters, which consist of the fitting vector of the objective function, i.e. K_1, K_2, K_3, K_4, K_5, a_1, a_2, a_3, a_4, a_5. For the gating dynamics, we are more interested in the processes of IP$_3$ binding, activating and inhibitory Ca^{2+} bindings, i.e., the parameters of K_1, K_5, and K_2. The parameter K_4 can be determined by $K_4 = K_1K_2/K_3$. Furthermore, we will not discuss the properties of parameters a_3 and a_4 in the paper, because a_3 and a_4 could not be determined from the observed quantities of P_O, τ_O and τ_C, as shown in equations (13)–(20). As a result, we just search for the optimal vector $X = (K_1, K_2, K_3, K_5, a_1, a_2, a_5)$ with seven parameters.

Considering the biologically reasonable values for each binding and dissociation constants, the possible ranges for parameters $(K_1, K_2, K_3, K_5, a_1, a_2, a_5)$ are set as follows: the lower limits are $(10^{-4}, 1, 10^{-4}, 10^{-4}, 10^{-4}, 10^{-4}, 10^{-4})$ and the upper limits are $(1, 10^4, 10^2, 1, 10^4, 1, 10^3)$ with unit μM for K_i and $\mu M^{-1}ms^{-1}$ for a_i, respectively. After we define the objective functions and constraint conditions of fitting vector, we run HIMO algorithm to get the optimal anti-bodies (the optimal vector) to minimize $F(X)$.

In order to test the efficiency of HIMO, we first consider a set of chosen parameters for IP$_3$R model to generate a series of P_O, τ_O and τ_C as the 'experimental data'. Then we apply the HIMO algorithm to fit the model parameters. In our simulation, the convergence condition of the immune algorithm is that the sum of the three mismatch functions in equations (21)–(23) (i.e., $W = W_{P_o} + W_{\tau_o} + W_{\tau_c}$) should be smaller than a critical number. Our simulation results show that with a smaller critical number, the obtained optimal parameters are closer to the chosen parameters, especially for those sensitive parameters in the model.

6. Results and discussions

6.1. Numerical fitting of Oo-IP$_3$R1, Oo-IP$_3$R3 and Sf-IP$_3$R

The experimental data of P_o, τ_o and τ_c against $[Ca^{2+}]$ at different $[IP_3]$ are given in figure 3 for Oo-IP$_3$R1 [6], Oo-IP$_3$R3 [7] and Sf-IP$_3$R [8] with different symbols. We apply HIMO algorithm to fit the model parameters. In our simulation, the convergence condition of the immune algorithm is that the sum of the three mismatch functions in equations (21)–(23) is smaller than 2.2, i.e. $W < 2.2$. In figure 3, as a comparison, the

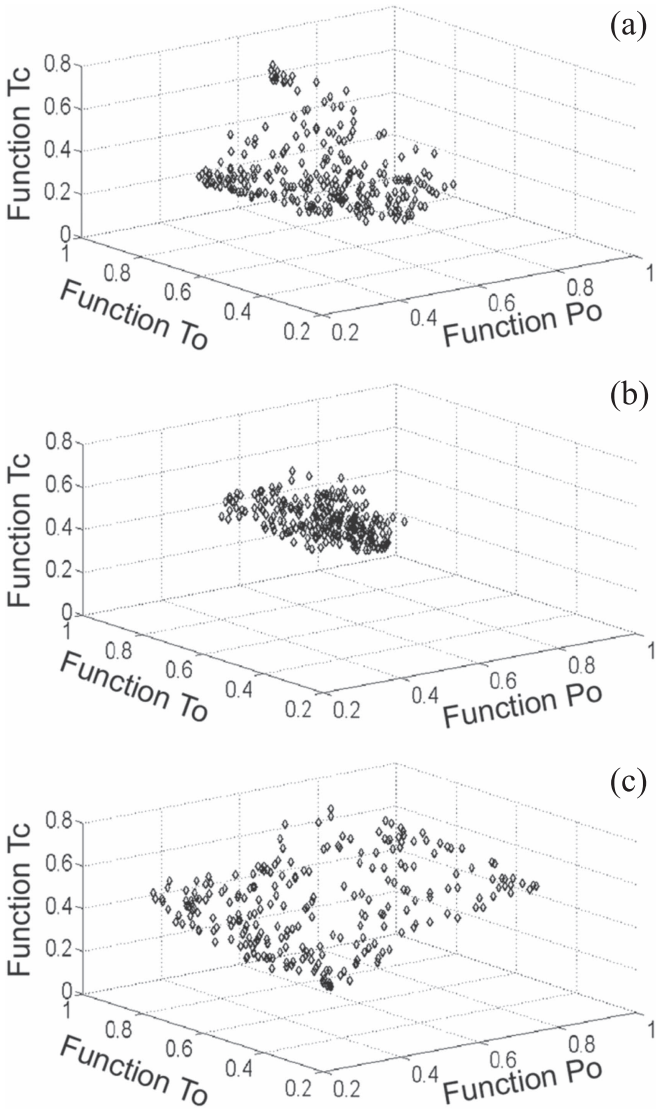

Figure 4. The Pareto-optimal front, i.e., the mismatch values of optimal parameters plotted in axes of W_{P_O}, W_{τ_O} and W_{τ_C} for (a) Oo-IP$_3$R1, (b) Oo-IP$_3$R3 and (c) Sf-IP$_3$R. Here only 250 points are plotted.

modeling curves with a set of optimal parameters are plotted for these three types of IP$_3$Rs.

Figure 3 shows that the immune algorithm can automatically find sets of model parameters to properly fit the experimental results. Some fittings are not perfect, such as that for τ_c in figure 3(b). This is because we did not apply the criteria that each of the three mismatch functions in equations (21)–(23) should be smaller than a small critical number in our simulation. Instead, the convergence condition of the immune algorithm here is that the sum of the three mismatch functions should be smaller than 2.2, which is a rather loose criterion. In fact, we found that the best fitting can give a value of W as small as 0.55. However, we are not trying to find out a set of best parameters to fit the experimental data, but to find many sets of good parameters and then to examine the distributions of these parameters. Thus, we consider a loose criterion with the critical number $W = 2.2$ which is four times of value of 0.55. We set 100 antibodies in the simulation, and so 100 sets of optimal parameters can be obtained for each searching process with the immune algorithm.

A large open time (~30 ms) for Sf-IP$_3$R does not mean that Sf-IP$_3$R must have a large K_2. In fact, we plot figure 3 with $K_2 = 82.5$, 18.65 and 27.6 μM for Oo-IP$_3$R1, Oo-IP$_3$R3, and Sf-IP$_3$R, respectively. Interestingly, a larger and a smaller K_2 applied for Oo-IP$_3$R1 and Oo-IP$_3$R3 both result in small open time. But a medium K_2 for Sf-IP$_3$R produces the large open time.

About 10 000 sets of optimal parameters were calculated for each of the three channels. Then with these optimal parameters, we can plot the Pareto-optimal front, which consists of all the dots plotted in the axes of the three mismatch functions of W_{P_O}, W_{τ_O} and W_{τ_C} with the optimal parameters. In figure 4, only 250 points randomly chosen from 10 000 points are plotted for each IP$_3$R for a clear view. The Pareto-optimal fronts obtained for Oo-IP$_3$R1 show more clustered dots with relatively small mismatch values

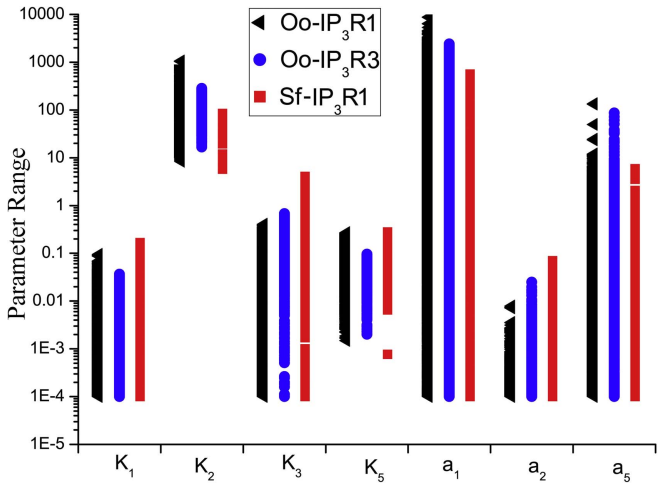

Figure 5. The scatter ranges of model parameters for Oo-IP$_3$R1 (triangles), Oo-IP$_3$R3 (circles) and Sf-IP$_3$R (squares).

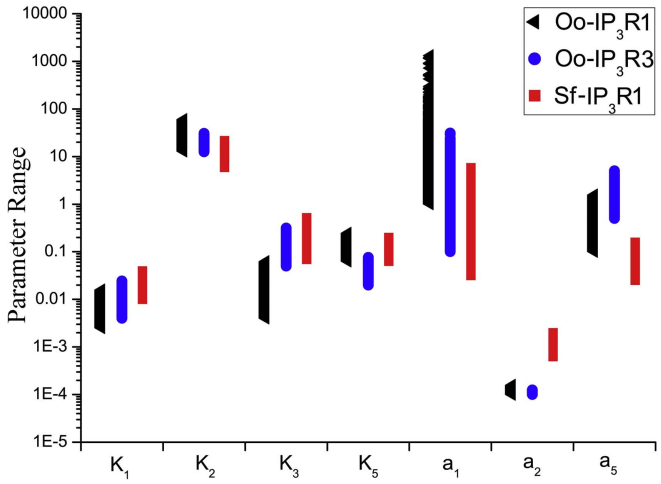

Figure 6. The scatter ranges of the filtered parameters for Oo-IP$_3$R1 (triangels), Oo-IP$_3$R3 (circles) and Sf-IP$_3$R (squares).

(figure 4(a)), while the Pareto-optimal fronts scatter more in space with large mismatch values for Sf-IP$_3$R (figure 4(c)).

6.2. Model parameter comparison among Oo-IP$_3$R1, Oo-IP$_3$R3 and Sf-IP$_3$R

For each type of IP$_3$R model, the distributing ranges with about 10 000 sets of optimal parameters are given in figure 5 for parameters of K_1, K_2, K_3, K_5, a_1, a_2 and a_5. The scatter ranges for the three IP$_3$R channels are quite similar.

Although each parameter scatters in a certain range, the 10 000 values show a certain probability distribution in the scatter range for each parameter. In detail, we calculate the distribution probability for parameters K_1, K_2, K_3, K_5, a_1, a_2 and a_5 against log(K_1), log(K_2), log(K_3), log(K_5), log(a_1), log(a_2) and log(a_5), respectively. To examine the robustness and reliability of model parameter, we delete all the sets of parameters in which distribution probability of any parameter is less than 5%. As a result, the remaining model parameter sets have >95% distribution probabilities for all seven parameters.

After this filtering process, only about 2000 sets of parameters remained for each channel type. The scatter ranges of the filtered parameters are plotted in figure 6 for Oo-IP$_3$R1, Oo-IP$_3$R3 and Sf-IP$_3$R. One can see that the parameter of a_1 is scattered over quite a large range for all three channels, indicating that a_1 is an insensitive parameter for gating dynamics. In other words, change of IP$_3$ binding rate in such a large range has little effect on channel behavior of P_o, τ_o or τ_c. The parameters of K_2 for Oo-IP$_3$R3, and a_2 for both Oo-IP$_3$R1 and Oo-IP$_3$R3 are confined in significantly narrower ranges, indicating that they are sensitive parameters for gating dynamics. So, P_O, τ_O and τ_C are sensitive to the values of K_2 and a_2.

Figure 6 indicates that the scatter range of parameter K_3 for Oo-IP$_3$R1 is quite different from that for Oo-IP$_3$R3 and Sf-IP$_3$R; the scatter range of parameter

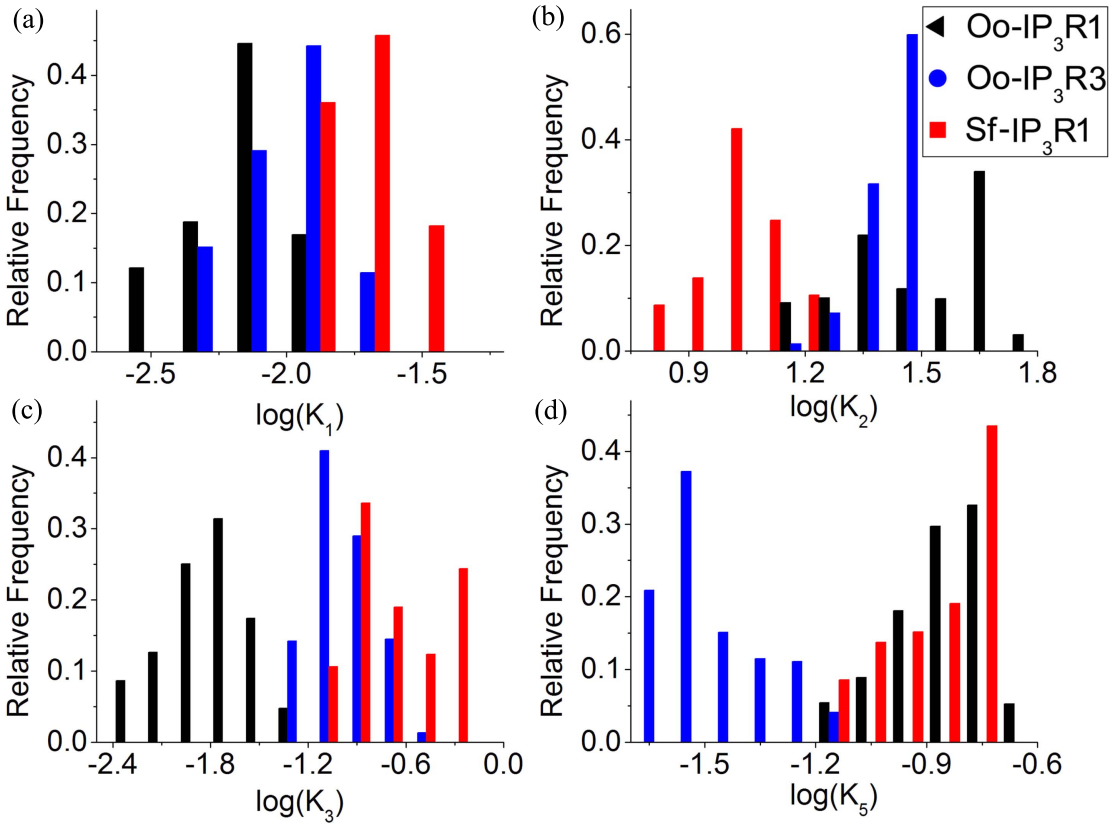

Figure 7. The comparison of probability distributions of the dissociation constants of (a) K_1, (b) K_2, (c) K_3, and (d) K_5 for Oo-IP$_3$R1 (black), Oo-IP$_3$R3 (blue) and Sf-IP$_3$R (red) models. All the bars in each figure correspond to the same range of log(K_i) for the three IP$_3$Rs. However, for a clear view, the bar width is smaller than the range length, and so the blue, red and black bars in the same range lie next to each other, rather than overlapping with each other.

a_2 for Sf-IP$_3$R is totally different from those for Oo-IP$_3$R1 and Oo-IP$_3$R3; and the scatter range of parameter a_5 for Sf-IP$_3$R is totally different from that for Oo-IP$_3$R3. Similar scatter ranges are observed for other parameters with the three IP$_3$Rs.

6.3. Comparison of disassociation constants among Oo-IP$_3$R1, Oo-IP$_3$R3 and Sf-IP$_3$R

Actually, the probability distribution of each parameter can reveal more information on the channel binding and unbinding dynamics. First, we discuss the probability distributions of the disassociation constants of IP$_3$R channels.

Figure 7(a) compares the probability distributions of dissociation constant K_1 among three types of IP$_3$Rs. In the model as shown in figure 2, K_1 represents the dissociation constant of IP$_3$ when the inhibitory Ca^{2+} binding site is not occupied. Figure 7(a) indicates that in order to open IP$_3$R the dissociation constant K_1 for IP$_3$-binding is typically around 0.01 μM for these three types of IP$_3$Rs. Thus, these three types of IP$_3$Rs show the similar open sensitivity in responding to [IP$_3$].

Figure 7(b) compares the probability distributions of dissociation constant K_2 among three types of IP$_3$Rs. In the model, K_2 represents the dissociation constant of inhibitory Ca^{2+} when IP$_3$ is binding to the subunit. Figure 7(b) shows that high [Ca^{2+}] around 30, 30, and 10 μM are required in order to inhibit the open Oo-IP$_3$R1, Oo-IP$_3$R3, and Sf-IP$_3$R, respectively. As a comparison, with a simple Hill equation fitting to experimental data, it has been suggested that typical dissociation constant K_2 should be around 59, 39, and 30 μM for Oo-IP$_3$R1, Oo-IP$_3$R3 and Sf-IP$_3$R, respectively (figure 7 in [3]), showing similar result of K_2 for these three IP$_3$Rs. Thus, the open Sf-IP$_3$R channel is easier to be inhibited than Oo-IP$_3$R1 and Oo-IP$_3$R3 in responding to high [Ca^{2+}].

Figure 7(c) plots the probability distributions of parameter K_3 which represents the dissociation constant of IP$_3$ when the inhibitory Ca^{2+} binding site is occupied. It shows that, when the channel is inhibited by Ca^{2+} ions, dissociation constants of [IP$_3$] are around 0.02, 0.16 and 0.16 μM for Oo-IP$_3$R1, Oo-IP$_3$R3 and Sf-IP$_3$R, respectively. This result indicates that the Ca^{2+}-inhibited states 001 and 011 can more easily jump to IP$_3$-bound states 101 and 111 for Oo-IP$_3$R1 than Oo-IP$_3$R3 and Sf-IP$_3$R in responding to the same [IP$_3$].

Figure 7(d) plots the probability distributions of parameter K_5 which represents the dissociation constant of active Ca^{2+} when inhibitory Ca^{2+} is not

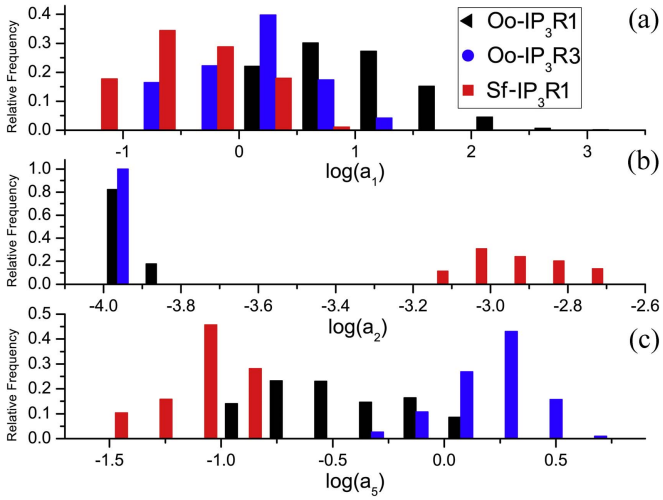

Figure 8. The comparison of probability distributions of binding rates of (a) a_1, (b) a_2, and (c) a_3, for Oo-IP$_3$R1 (black), Oo-IP$_3$R3 (blue) and Sf-IP$_3$R (red) models. All the bars correspond to the same range of log(a_i) for the three IP$_3$Rs. However, for a clear view, the bar width is smaller than the range length, and so the blue, red and black bars in the same range lie next to each other, rather than overlapping with each other.

bound to the subunit. In order to open IP$_3$R channel the dissociation constants K_5 for [Ca^{2+}] are about 0.13, 0.04, and 0.13 μM for Oo-IP$_3$R1, Oo-IP$_3$R3 and Sf-IP$_3$R, respectively. As a comparison, it has been suggested by Hill equation fitting to the experimental data that typical dissociation constant K_5 should be around 0.25, 0.077, and 0.25 μM for Oo-IP$_3$R1, Oo-IP$_3$R3 and Sf-IP$_3$R, respectively (figure 7 in [3]), showing similar result of K_5 for these three IP$_3$Rs. This result indicates that Oo-IP$_3$R3 channel is easier to open than Oo-IP$_3$R1 and Sf-IP$_3$R in responding to low [Ca^{2+}].

6.4. Comparison of binding rates among Oo-IP$_3$R1, Oo-IP$_3$R3 and Sf-IP$_3$R

In figure 8, the probability distributions of binding constants a_1, a_2, and a_5 are plotted and compared. The parameter a_1 defines the binding rate of IP$_3$ onto the subunit when the inhibitory Ca^{2+} binding site is not occupied. Although the scatter ranges of parameter a_1 given in figure 6 suggest that the binding rates may be typically large for Oo-IP$_3$R1 and small for Sf-IP$_3$R, figure 8(a) shows an overlap of binding rate around 2 $\mu M^{-1}ms^{-1}$ with large probability for these three types of IP$_3$Rs. This result indicates that the IP$_3$ binding rate a_1 could be quite similar among Oo-IP$_3$R1, Oo-IP$_3$R3 and Sf-IP$_3$R channels.

We have concluded from figure 7(a) that the 3 types of IP$_3$Rs show the similar open sensitivity in responding to IP$_3$ messenger. As a result, when the inhibitory Ca^{2+} binding site is not occupied, the IP$_3$ binding and unbinding rates could be quite similar among Oo-IP$_3$R1, Oo-IP$_3$R3 and Sf-IP$_3$R channels.

The parameter a_2 defines the binding rate of Ca^{2+} to inhibit the subunit when IP$_3$ is binding to the subunit. Figure 8(b) points out that Oo-IP$_3$R1 and Oo-IP$_3$R3 have the same binding rate around 10^{-4} $\mu M^{-1}ms^{-1}$, which is slower than that of Sf-IP$_3$R (around 10^{-3} $\mu M^{-1}ms^{-1}$). As observed from figure 7(b), Sf-IP$_3$R channel has a smaller dissociation constant K_2 than Oo-IP$_3$R1 and Os-IP$_3$R3. These data indicate that, among these three types of IP$_3$R channels, Sf-IP$_3$R has the faster unbinding rate for inhibitory Ca^{2+}, while Oo-IP$_3$R1 and Oo-IP$_3$R3 have the similar slow unbinding rate for inhibitory Ca^{2+}.

The parameter a_5 defines the binding rate of Ca^{2+} to activate the subunit when inhibitory Ca^{2+} is not bound to the subunit. Figure 8(c) shows that, among these three channels, Oo-IP$_3$R3 has a fast activating Ca^{2+} binding rate (around 2 $\mu M^{-1}ms^{-1}$), while Sf-IP$_3$R has a slow activating Ca^{2+} binding rate (around 0.1 $\mu M^{-1}ms^{-1}$). A middle binding rate around 0.4 $\mu M^{-1}ms^{-1}$ is suggested for Oo-IP$_3$R1.

As a result, the representative ranges for model parameters of K_1, K_2, K_3, K_5, a_1, a_2 and a_5 are listed in table 1 for Oo-IP$_3$R1, Sf-IP$_3$R and Oo-IP$_3$R3.

Table 1. The parameter ranges of Oo-IP$_3$R1, Sf-IP$_3$R and Oo-IP$_3$R3.

Parameters	Oo-IP$_3$R1	Oo-IP$_3$R3	Sf-IP$_3$R
$K_1\mu M$	0.002–0.02	0.004–0.025	0.01–0.04
K_2	10–65	13–35	6–20
K_3	0.005–0.06	0.05–0.3	0.07–0.5
K_5	0.06–0.25	0.02–0.07	0.06–0.2
$a_1\mu M^{-1}ms^{-1}$	1–200	0.1–20	0.05–5
a_2	1×10^{-4}–1.6×10^{-4}	1×10^{-4}–1.3×10^{-4}	6×10^{-4}–0.002
a_5	0.1–1.5	0.5–5	0.03–0.16

7. Conclusion

IP$_3$R channels play a pivotal role in converting extracellular stimuli into intracellular Ca^{2+} signals, which regulate almost all cellular processes [3, 36].

Different from the typical procedure of channel modeling with only a set of parameters [7, 8, 12–14, 17] to describe the channel dynamics, in this paper we apply the HIMO immune algorithm to fit the parameters of a modified DYK IP_3R model based on the experimental data of nuclear membrane patch clamp for Oo-IP_3R1, Oo-IP_3R3 and Sf-IP_3R, and fitting the open probability, mean open time and mean close time, a mass of optimal parameters have been obtained with the immune algorithm. Through contrastive analysis of probability distributions of parameters, the different binding and unbinding dynamics with Ca^{2+} and IP_3 have been studied and compared in detail among these three types of IP_3Rs. Our results provide insights about the relation between the observed gating characteristics and the gating parameters in different IP_3Rs.

For IP_3R gating dynamics, the most important processes are the binding of IP_3 and Ca^{2+} to open the channel and the binding of Ca^{2+} to inhibit the channel, i.e., the processes related to K_1, K_5, and K_2 shown in figure 2. We show that these three IP_3Rs have the similar open sensitivity in response to $[IP_3]$. In detail, in the case that the inhibitory Ca^{2+} binding site is not occupied, the IP_3 binding and unbinding rates to the subunit could be quite similar among Oo-IP_3R1, Oo-IP_3R3 and Sf-IP_3R channels. Among these three IP_3Rs, Oo-IP_3R3 channel is easier to be open than Oo-IP_3R1 and Sf-IP_3R in responding to low $[Ca^{2+}]$, because Oo-IP_3R3 has a faster activating Ca^{2+} binding rate than Oo-IP_3R1 and Sf-IP_3R. Our data indicate that the open Sf-IP_3R channel is easier inhibited than Oo-IP_3R1 and Oo-IP_3R3 in responding to high $[Ca^{2+}]$. Among these three channels, Sf-IP_3R not only has a fast binding rate for inhibitory Ca^{2+} to bind to the active subunit, but also has a fast unbinding rate for inhibitory Ca^{2+}.

Our results reveal that the Ca^{2+} activation and inhibition properties are different for these three channels. Especially, the Oo-IP_3R3 channel is easy to open in responding to low $[Ca^{2+}]$, while Sf-IP_3R channel is easily inhibited in responding to high $[Ca^{2+}]$. Therefore, they will have distinctive spatiotemporal characteristics of IP_3-induced Ca^{2+} oscillations. The slight differences in the Ca^{2+} signaling patterns in some cases can critically affect the final cellular decision for survival or death [1, 5]. As most cell types expressing more than one subtype IP_3R, the integrative effects of the different types of IP_3Rs expressed in a cell on intracellular Ca^{2+} oscillations need to be further investigated.

Different from the usual way to find one set of parameter to best fit the experimental data and then to discuss the channel dynamics, here we are trying to find many sets of good parameters and then to examine their distribution properties. Such a discussion can reveal the sensitivity of each parameter on channel gating dynamics. In order to do so, we consider a loose criterion for the sum of three mismatch functions in the immune algorithm. As a result, the fitting quality is not perfect and the scatter is large, as shown in figure 5. But after filtering out the parameters with small probability, the remained parameters are representative. Some parameters then cluster in narrow ranges, but others still scatter in wide ranges. The widely scattered parameters just indicate that the gating dynamics of P_O, τ_O and τ_C are less sensitive to these parameters. As an extreme case, the gating dynamics of P_O, τ_O and τ_C is totally independent of a_3 and a_4, meaning that the simulating results will give homogenous distribution scattering on the whole parameter space for a_3 and a_4.

By considering the modeling parameter distribution, we find that the rate a_1 for IP_3 binding onto the subunit scatters in quite a large range for all these channels, indicating that the IP_3 binding rate is not a sensitive parameter for stationary gating dynamics. In other words, the change of IP_3 binding rate even in such a large range has little effect on the channel behavior of P_O, τ_O and τ_C. The parameters of the dissociation constant K_2 of inhibitory Ca^{2+} for Oo-IP_3R3 and the binding rate a_2 of Ca^{2+} to inhibit the subunit for both Oo-IP_3R1 and Oo-IP_3R3 cluster in narrow ranges, indicating that inhibitory Ca^{2+} binding/unbinding rates are sensitive parameters for gating dynamics. As a result, the channel properties of P_O, τ_O and τ_C are sensitive to the values of K_2 and a_2 for Oo-IP_3Rs.

In this paper, the IP_3R channel properties are discussed and analyzed based on a modified DYK model which was developed by considering only the most basic three characteristics in IP_3R gating dynamics, i.e. P_O, τ_O and τ_C. Other behaviors of channel gating, including modal gating [25] and kinetic response to changes in ligand concentrations [9], indicate that complex cooperativity could exist among different IP_3R subunits and between IP_3 and high-affinity Ca^{2+} binding sites [17, 37]. Considering the limits of the modified DYK model used in this study, one may question the validity of our conclusions drawn from the simulations solely on the DYK model. If, as still a challenge for IP_3R modeling, there is a full model which can describe all these gating dynamics, one can certainly find some parameters or expressions to describe the binding/unbinding dynamics of Ca^{2+}-activation, Ca^{2+}-inhibition and IP_3 activation. In other words, with such a full model, one can still define the effective binding/unbinding rates for these Ca^{2+}/IP_3 binding/unbinding processes. We suggest that these binding/unbinding rates predicted by different models should be more or less similar, because they actually describe the same processes. Thus, our conclusions on these effective binding/unbinding properties should still be valid. As an example, our conclusions on the comparison of K_2 and K_5 for three IP_3Rs are quite similar as those given by some simple Hill equation fittings to the same experimental data [3].

The ultimate goal of developing kinetic models to describe the single IP_3R channel behaviors is to

simulate the behavior of IP_3R channels in ligand conditions and to discuss the kinetic behavior of cytosolic Ca^{2+} signals. One may propose that the sensitive channel parameters could play important role in generating the spatially and temporally complex Ca^{2+} oscillations in the cytosol. Thus, an interesting question for further investigation is how a small change of sensitive channel parameter could cause a large kinetic variation on Ca^{2+} oscillations. We also suggest that the immune algorithm can be applied to the parameter sensitivity discussion in other biological systems.

Acknowledgments

This work was supported by the National Natural Science Foundation of China under grant 11504214 and 31370830, the Fujian Province Funds for Leading Scientist in Universities and Shenzhen Technology Plan under Grant JCYJ20140418095735608.

References

[1] Berridge M, Bootman M and Lipp P 1998 Calcium-a life and death signal *Nature* **395** 645–8
[2] Berridge M, Lipp P and Bootman M 2000 The versatility and universality of calcium signalling *Nat. Rev. Mol. Cell Biol.* **1** 11–21
[3] Foskett J K, White C, Cheung K H and Mak D O D 2007 Inositol trisphosphate receptor Ca^{2+} release channels *Physiol. Rev.* **87** 593–658
[4] Zhang S, Fritz N, Ibarra C and Uhlén P 2011 Inositol 1, 4, 5-trisphosphate receptor subtype-specific regulation of calcium oscillations *Neurochem. Res.* **36** 1175–85
[5] Ivanova H, Vervliet T, Missiaen L, Parys J B, De Smedt H and Bultynck G 2014 Inositol 1, 4, 5-trisphosphate receptor-isoform diversity in cell death and survival *Biochim. Biophys. Acta Mol. Cell Res.* **1843** 2164–83
[6] Mak D-O D, McBride S and Foskett J K 1998 Inositol 1, 4, 5-tris-phosphate activation of inositol tris-phosphate receptor Ca^{2+} channel by ligand tuning of Ca^{2+} inhibition *Proc. Natl Acad. Sci. USA* **95** 15821–5
[7] Mak D-O D, McBride S M and Foskett J K 2003 Spontaneous channel activity of the inositol 1, 4, 5-trisphosphate ($InsP_3$) receptor ($InsP_3R$), application of allosteric modeling to calcium and $InsP_3$ regulation of $InsP_3R$ single-channel gating *J. Gen. Physiol.* **122** 583–603
[8] Ionescu L, Cheung K H, Vais H, Mak D O D, White C and Foskett J K 2006 Graded recruitment and inactivation of single $InsP_3$ receptor Ca^{2+}-release channels: implications for quartal Ca^{2+} release *J. Physiol.* **573** 645–62
[9] Mak D O D, Pearson J E, Loong K P C, Datta S, Fernández-Mongil M and Foskett J K 2007 Rapid ligand-regulated gating kinetics of single inositol 1, 4, 5-trisphosphate receptor Ca^{2+} release channels *EMBO Rep.* **8** 1044–51
[10] Bezprozvanny I, Watras J and Ehrlich B E 1991 Bell-shaped calcium-response curves of Ins (1, 4, 5) P_3-and calcium-gated channels from endoplasmic reticulum of cerebellum *Nature* **351** 751–4
[11] Hagar R E, Burgstahler A D, Nathanson M H and Ehrlich B E 1998 Type III $InsP_3$ receptor channel stays open in the presence of increased calcium *Nature* **396** 81–4
[12] Sneyd J and Dufour J-F 2002 A dynamic model of the type-2 inositol trisphosphate receptor *Proc. Natl Acad. Sci. USA* **99** 2398–403
[13] Dupont G and Combettes L 2006 Modelling the effect of specific inositol 1, 4, 5-trisphosphate receptor isoforms on cellular Ca^{2+} signals *Biol. Cell* **98** 171–82
[14] De Young G W and Keizer J 1992 A single-pool inositol 1, 4, 5-trisphosphate-receptor-based model for agonist-stimulated oscillations in Ca^{2+} concentration *Proc. Natl Acad. Sci. USA* **89** 9895–9
[15] Shuai J W, Pearson J E, Foskett J K, Mak D-O D and Parker I 2007 A kinetic model of single and clustered IP_3 receptors in the absence of Ca^{2+} feedback *Biophys. J.* **93** 1151–62
[16] Shuai J W, Yang D, Pearson J and Rüdiger S 2009 An investigation of models of the IP_3R channel in *Xenopus* oocyte *Chaos* **19** 037105
[17] Ullah G, Mak D-O D and Pearson J E 2012 A data-driven model of a modal gated ion channel: the inositol 1, 4, 5-trisphosphate receptor in insect Sf9 cells *J. Gen. Physiol.* **140** 159–73
[18] Keizer J and De Young G 1994 Simplification of a realistic model of IP_3-induced Ca^{2+} oscillations *J. Theor. Biol.* **166** 431–42
[19] Wang C and Zhao Y 2008 A new fault detection method based on artificial immune systems *Asia Pac. J. Chem. Eng.* **3** 706–11
[20] Wang W, Gao S and Tang Z 2009 Improved pattern recognition with complex artificial immune system *Soft Comput.* **13** 1209–17
[21] Ramakrishnan S and Srinivasan S 2009 Intelligent agent based artificial immune system for computer security—a review *Artif. Intell. Rev.* **32** 13–43
[22] Yoo J and Hajela P 1999 Immune network simulations in multicriterion design *Struct. Optim.* **18** 85–94
[23] Gong M G, Jiao L C, Du H F and Bo L F 2008 Multiobjective immune algorithm with nondominated neighbor-based selection *Evol. Comput.* **16** 225–55
[24] Chen J Y, Lin Q Z and Ji Z 2010 A hybrid immune multiobjective optimization algorithm *Eur. J. Oper. Res.* **204** 294–302
[25] Lin Q Z and Chen J Y 2013 A novel micro-population immune multiobjective optimization algorithm *Comput. Oper. Res.* **40** 1590–601
[26] Freschi F and Repetto M 2005 Multiobjective optimization by a modified artificial immune system algorithm *Lecture Notes in Computer Science* vol 3627 pp 248–61
[27] Freschi F and Repetto M 2006 Vis: an artificial immune network for multi-objective optimization *Eng. Optim.* **38** 975–96
[28] Gao J Q and Wang J 2010 WBMOAIS: a novel artificial immune system for multiobjective optimization *Comput. Oper. Res.* **37** 50–61
[29] Cutello V, Narzisi G and Nicosia G 2005 A class of pareto archived evolution strategy algorithms using immune inspired operators for Ab-Initio protein structure prediction *Lecture Notes in Computer Science* vol 3449, pp 54–63
[30] Tan K C, Goh C K, Mamun A A and Ei E Z 2008 An evolutionary artificial immune system for multi-objective optimization *Eur. J. Oper. Res.* **187** 371–92
[31] Wong E Y C, Yeung H S C and Lau H Y K 2009 Immunity-based hybrid evolutionary algorithm for multi-objective optimization in global container repositioning *Eng. Appl. Artif. Intell.* **22** 842–54
[32] Lin Q Z, Chen J Y, Zhan Z H, Chen W N, Coello C A, Yin Y L, Lin C M and Zhang J 2016 A hybrid evolutionary immune algorithm for multiobjective optimization problems *IEEE Trans. Evolutionary Comput.* in press (doi:10.1109/TEVC.2015.2512930)
[33] Deb K and Agrawal R B 1995 Simulated binary crossover for continuous search space *Complex Syst.* **9** 115–48
[34] Rüdiger S, Jung P and Shuai J W 2012 Termination of Ca^{2+} release for clustered IP_3R channels *PLoS Comp. Biol.* **8** e1002485
[35] Qi H, Huang Y, Rüdiger S and Shuai J W 2014 Frequency and relative prevalence of calcium blips and puffs in a model of small IP_3R clusters *Biophys. J.* **106** 2353–63
[36] Mikoshiba K 2007 The IP_3 receptor/Ca^{2+} channel and its cellular function *Biochem. Soc. Symp.* **74** 9–22
[37] Ionescu L, White C, Cheung K H, Shuai J W, Parker I, Pearson J E, Foskett J K and Mak D O D 2007 Mode switching is the major mechanism of ligand regulation of InsP3 receptor calcium release channels *J. Gen. Physiol.* **130** 631–45